

RESEARCH ARTICLE

Real-time wind field reconstruction from LiDAR measurements using a dynamic wind model and state estimation

P. Towers and B. Li. Jones

Department of Automatic Control and Systems Engineering, The University of Sheffield, Sheffield, S1 3JD, UK

ABSTRACT

The use of light detection and ranging (LiDAR) instruments offer many potential benefits to the wind energy industry. Although much effort has been invested in developing such instruments, the fact remains that they provide limited spatio-temporal velocity measurements of the wind field. Moreover, LiDAR measurements only provide the radial (line-of-sight) velocity component of the wind, making it difficult to precisely determine wind magnitude and direction, owing to the so-called ‘cyclops’ dilemma. Motivated by a desire to extract more information from typical LiDAR data, this paper aims to show that it is possible to accurately estimate, in a real-time fashion, the radial and tangential velocity components of the wind field. We show how such reconstructions can be generated through the synthesis of an unscented Kalman filter that employs a low-order dynamic model of the wind to estimate the unmeasured velocities within the wind field, using repeated measurement updates from typical nacelle-mounted LiDAR instruments. This approach is validated upon synthetic data generated from large eddy simulations of the atmospheric boundary layer. The accuracy of the wind field estimates are validated across a variety of beam configurations, look directions, atmospheric stabilities and imperfect measurement conditions. The main outcome of this paper is a technique that offers the potential to accurately reconstruct wind fields from LiDAR data, overcoming the cyclops dilemma in the process. The ultimate aim of this research is to provide reliable gust detection warning systems to offshore construction workers, in addition to accurate wind field estimates for use in preview turbine pitch control systems. © 2014 The Authors. *Wind Energy* published by John Wiley & Sons Ltd.

KEYWORDS

LiDAR; fluid dynamics; gust detection; Cyclops dilemma; real-time estimation

Correspondence

B. Li. Jones, Department of Automatic Control and Systems Engineering, The University of Sheffield, Sheffield, S1 3JD, UK.
E-mail: b.l.jones@sheffield.ac.uk

This is an open access article under the terms of the Creative Commons Attribution License, which permits use, distribution and reproduction in any medium, provided the original work is properly cited.

Received 9 May 2014; Revised 29 October 2014; Accepted 2 November 2014

1. INTRODUCTION

The offshore wind energy industry is currently experiencing significant growth with sustained multi-national political backing to provide a growing source of renewable energy. In turn, this has led to major investment in offshore wind technology, for which improvements in the economic efficiency of energy production have been the principal driving force. Numerous factors contribute to the overall cost of energy, and many of these are adversely affected by the inherent unsteadiness of the wind. For example, construction and maintenance operations, as well as the individuals who perform them, such as rope access workers, are particularly vulnerable to violent gusts of wind that can strike at any time and with no advance warning. In the interests of health and safety, construction and maintenance crew must therefore operate in a more conservative fashion than would otherwise be necessary were advance knowledge of oncoming gusts available. Meteorological forecasts typically only provide averaged wind speeds over a large area and are thus of insufficient fidelity to resolve the smaller spatial and faster temporal dynamics of typical wind gusts. Such gusts are also a primary cause of the extreme and fatigue loads that lead to greater construction costs, in the form of stronger and heavier towers, as well as increased maintenance activity and lower operational life expectancy. Indeed, a report published by the European Wind

Energy Association¹ stated that technologies to improve turbine reliability were of ‘key’ importance, given the considerable financial cost of repair and maintenance at remote offshore locations.

With this in mind, the ability to sample an oncoming wind field has been made possible in recent years with the advent of light detection and ranging (LiDAR) instruments. Such instruments now possess sufficient bandwidth and ranging capability to enable fast and accurate radial velocity measurements at a range of locations from a turbine.^{2,3} However, the question of how best to use these measurements to detect an oncoming gust remains open, as does the question of how best to incorporate such information for use within a preview control scheme (e.g.^{4,5,6,7}). The success of such controllers will inevitably be reliant upon the accuracy of the predictions of the incident wind field. Such predictions will depend not only upon the quality of the LiDAR measurements, but also upon the accuracy of any model used firstly to link the measurements to regions of the flow that are not directly sampled and secondly to evolve the present wind field forwards in time. Although the wind is a complex and dynamic phenomenon that varies considerably with height within the atmospheric boundary layer, nearly all design and control within the wind energy industry is based on an assumption of uniform and steady flow across the rotor plane.⁸ Such assumptions become increasingly erroneous as wind turbines protrude higher into the atmospheric boundary layer. As an example, low-level nocturnal jets of air that create a non-uniform wind distribution across the rotor plane are leading to significant repair and maintenance activity upon commercial turbines.⁸ In addition, the presence of complex turbulent structures of spatial scales smaller than those of the rotor can lead to uneven loading, resulting in wear or damage to the turbine structure.^{9,10} Simulations of the atmospheric boundary layer provide a convenient means of visualising the non-uniformity of the wind across the rotor plane. An example of such non-uniformity is shown in Figure 1, which displays a typical snapshot of the wind field taken in the horizontal plane at a height of 85 m above the sea surface. Low and high-speed features with length scales smaller than a rotor diameter are clearly present and thus need to be detected in the oncoming flow if one is interested in developing LiDAR-based preview control.

The extent to which such spatio-temporal unsteadiness can be detected via existing LiDAR technology and associated signal processing schemes is unclear at present, but a growing body of research is beginning to address this issue. An experimental study¹¹ presented the application of single-beam LiDAR for measuring the oncoming wind characteristics, for ranges up to 200 m. According to the authors, this was the first time a LiDAR instrument had been attached to the nacelle of a wind turbine for monitoring of the oncoming flow. A further experimental study¹² was presented, comparing measurements taken by a prototype LiDAR and a sonic anemometer at the same location. The wind turbine was yawed at 283° (from due north), and for wind directions between 280° and 290° the devices were in good agreement. However, following a change in the wind direction to around 160°, the observed LiDAR speed fell and was not in agreement with the anemometer. As the angle between the line-of-sight of the LiDAR and the actual wind direction grew, the projection of the wind speed upon the line-of-sight decreased, resulting in a loss of accuracy. Such difficulty in resolving wind direction and magnitude from line-of-sight velocity data is commonly referred to as the ‘cyclops’ dilemma, and has been reported by several authors.^{4,13,14} Extra information is therefore required in order to resolve wind magnitude and direction from line-of-sight velocity measurements and as will be shown in this paper, such information may be teased out from a physical model that captures the spatio-temporal dynamics of the wind.

The simplest of such models are based upon Taylor’s frozen turbulence hypothesis,¹⁵ where the spatial structure of turbulent wind gusts remains unchanged as they advect with the mean wind speed. Consequently, much of the existing literature on LiDAR-assisted control of wind turbines⁷ and LiDAR-based wind field reconstruction,¹⁶ has employed some form of Taylor’s frozen turbulence hypothesis. In the present work, we seek to estimate the wind field not just at a point

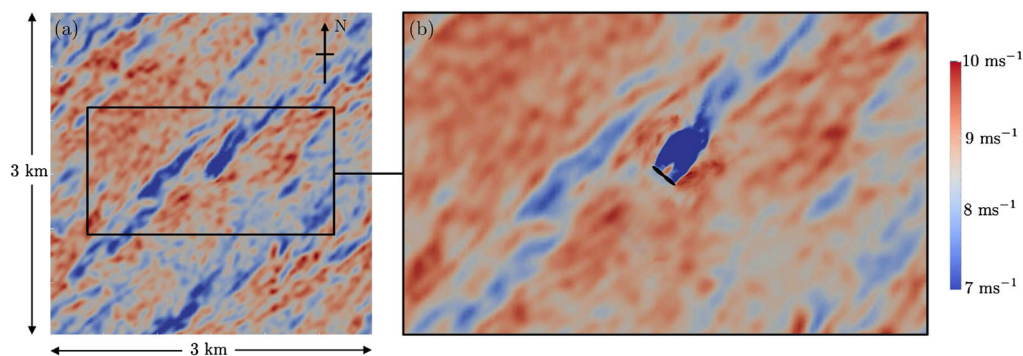


Figure 1. Typical snapshot from a large eddy simulation of the atmospheric boundary layer at a height of 85 m above sea level, with a mean windspeed of 8.5 m s^{-1} . Figure (a) shows the spatial variation of gusts within a 3 km square domain with a wind turbine generator located at the centre, whilst Figure (b) shows a close-up of the flow around this turbine, with the rotor plane drawn in black.

Coloured regions indicate wind magnitude and the prevailing wind direction is from the southwest.

location, but within a region spanned by two LiDAR beams, in order to determine a fuller picture of the oncoming wind field. Selecting a model suitable for this task represents a compromise between model accuracy and model complexity. The most accurate models are those that employ the Navier–Stokes equations,¹⁷ but these are too complex for the purpose of computing real-time predictions on low-cost hardware. The derivation of a suitable model is thus a central contribution of this paper and we note that other authors, e.g.¹⁸ have developed other simplified wind models. Importantly, the resulting model is dynamic, in the sense that it describes how the wind field evolves over time. This enables knowledge of past wind field information, obtained from a temporal history of LiDAR measurements, to be incorporated into current and future estimates of the wind field. The key enabler in this respect is the use of model-based state estimation techniques from the control systems community. In this paper, an unscented Kalman filter¹⁹ is used to reduce, in a recursive fashion, the error between actual and estimated wind fields. To the best of our knowledge, this work is the first to use such Kalman filtering techniques to reconstruct the wind field upstream from a turbine, using measurements from a typical LiDAR instrument. As such, this work combines elements from wind energy, fluid dynamics and control systems engineering.

The remainder of this paper is structured as follows. Section 2 provides a description of the problem addressed, specifically the design of a state estimator to reconstruct the wind field spanned by two horizontal LiDAR beams. A description of the simulation environment employed to generate synthetic wind fields is also described in this section. State estimators employ models of the systems whose states they are attempting to reconstruct, and so Section 3 describes the derivation of the dynamic wind model employed in this work. This section also describes the scale analysis and spatio-temporal discretization used to simplify the estimation model. The unscented Kalman filter that employs this simplified model is described in Section 4, along with some remarks concerning the real-time feasibility of this approach. Results that demonstrate the efficacy of the proposed wind field reconstruction scheme across a range of operating scenarios are presented in Section 5. Finally, the conclusions of this work and future directions are presented in Section 6.

2. PROBLEM DESCRIPTION

The problem addressed in this paper is summarized in Figure 2. Starting from the top-left of this figure, a nacelle-mounted, dual-beam LiDAR instrument samples the true wind field, in a horizontal plane 85m above sea level at regularly spaced intervals in time. The LiDAR instrument considered in this work samples the radial velocity component at 10 regularly spaced ranges along each beam (red circles), from 40 m to 220 m, at a sampling rate of 1 Hz. Two different cases are considered based on beam half angles of 15° and 30°. The measurements are stacked into a measurement vector y_k , where $k = 0, 1, 2, \dots$ denotes the sample instant. The measurement vector is then fed into a processing unit that executes a state estimation algorithm, described in further detail in the succeeding discussion.

2.1. State estimation of dynamic systems

In the interests of simplicity, it is sufficient at this point to define the states of our system as the radial and azimuthal wind velocities at discrete locations within a conical sector containing two horizontal LiDAR beams. The formal definitions of

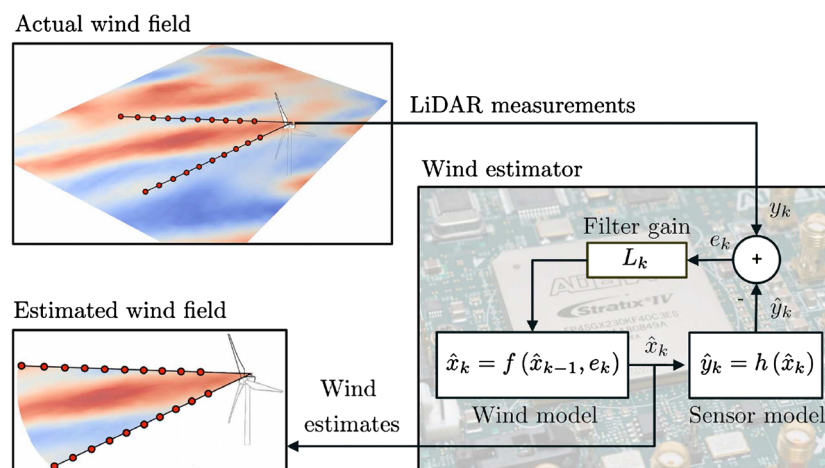


Figure 2. Problem schematic.

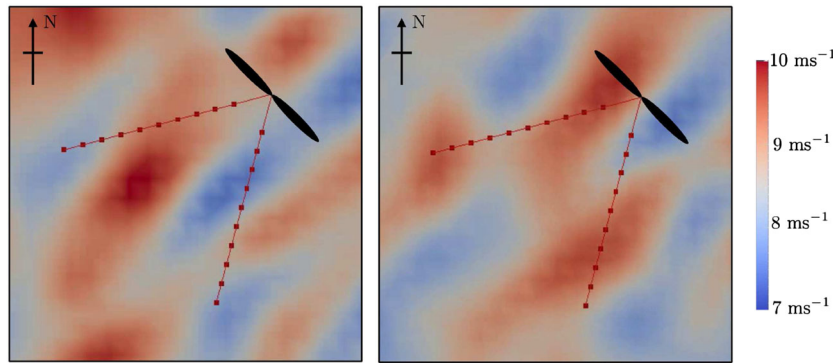


Figure 3. Snapshots of the wind field moving through the plane of the LiDAR beams (red lines) with a mean speed of 8.5 ms^{-1} . The direction of flow is from the southwest. The two images are separated by a time interval of 10 s, during which time the wind field is sampled on ten occasions, which is sufficiently fast to resolve typical gusts as they traverse the beams. The LiDAR range is 220 m, and the distance between sample points (red squares) is 20 m, which is significantly less than the characteristic gust length scales ($\mathcal{O}(10^2)\text{m}$). Rotor planes have been drawn on these figures to aid clarity, but note that turbine dynamics are not included in the present work.

the states and their spatial locations are described in Section 3.2.2. At each sample instant, the states are stacked into a vector x_k , and the role of the state estimator is to produce state estimates \hat{x}_k that are in close agreement with the actual states. In order to achieve this, the estimator employs a wind model (derived in Section 3) that acts as a one-step-ahead predictor, taking in the estimates from the previous time step \hat{x}_{k-1} and evolving these forward in time to yield the current estimate \hat{x}_k . A sensor model then uses these state estimates to form estimates of the current measurements \hat{y}_k . In the present work, the measurements are a subset of the states of the wind field, specifically the radial velocity components at the previously defined ranges along the LiDAR beams. The estimated measurements are then subtracted from the actual measurements to form an error vector e_k . This is multiplied by the filter gain L_k (a matrix) to produce a correction term that is introduced into the wind model in an attempt to reduce the error in subsequent iterations. At each iteration of the estimation algorithm, a new filter gain is computed in order to minimize the mean square state estimation error, $\mathcal{E} \left\{ (x_k - \hat{x}_k) (x_k - \hat{x}_k)^T \right\}$, where $\mathcal{E}\{\cdot\}$ denotes the expectation of a sequence and $(\cdot)^T$ is the vector transpose, given all measurements up to and including the current sample. This is the standard objective of the celebrated Kalman filter [20–24]. The state estimates can then be plotted to yield the estimated wind field, shown in the lower left of Figure 2.

A few remarks are in order at this point. Firstly, the LiDAR instrument under consideration in the present work was chosen to resolve the spatio-temporal scales of the large scale structures within the atmospheric boundary layer at a typical mean wind speed of 8.5 m s^{-1} . Figure 3 shows two snapshots, taken 10 seconds apart, of a typical simulated wind field, from which it is reasonable to expect that the present spatio-temporal sampling is sufficient to detect oncoming gusts. Secondly, the domain of estimation is a conical region of half-angle 30° and radius 220 m, based on a typical LiDAR configuration offered by the likes of the Avent Wind Iris, for example. Other LiDAR configurations may ultimately provide better or worse wind field reconstructions, but such considerations are beyond the scope of the present work. Lastly, the wind model employed in the estimator requires an initial state estimate \hat{x}_0 . In the absence of any initial knowledge of the actual wind field, an initial estimate corresponding to a quiescent wind field (all velocities equal to zero) is assumed.

The manner in which data from realistic wind fields is obtained for use in this study is described in the following section.

2.2. Large eddy simulations of the atmospheric boundary layer

The wind field data in this study is generated from the Simulator for Offshore Wind Farm Applications (SOWFA) [25–27] and is based on the Open Source Field Operation and Manipulation (OpenFOAM) (OpenCFD Ltd., Bracknell, Berkshire, UK) C++ libraries. The solver enables simulation of the atmospheric boundary layer under neutral (wind and water at the same temperature) and unstable (wind cooler than water) stability conditions. Wind fields are generated in a domain of $3 \times 3 \times 1$ kilometres in the latitudinal, longitudinal and vertical directions respectively. Spatial scales are resolved to 10m in all directions, and the wind fields are advanced with a variable time step, second-order backwards difference scheme that maintains a maximum Courant number of 0.75. Turbine dynamics can also be included as part of a secondary simulation, as shown in Figure 1, for example, but in the interests of simplicity will not be considered henceforth in this work. The boundary conditions at the planetary surface are those of,²⁸ whilst shear stress and temperature flux are set to zero at the upper boundary. Further details are described in.²⁷

3. DYNAMIC WIND MODELS

The aim of this section is to derive a simplified model of the wind dynamics for use as part of a state estimation scheme. Our starting point is a model that describes the evolution of the velocity field within the atmospheric boundary layer, similar to the model used, for example, within the SOWFA simulations.

3.1. The atmospheric boundary layer equations

Owing to the geometry of the LiDAR beams, we choose to work in a polar coordinate system defined by radial r , azimuthal ψ and vertical z directions. The atmospheric boundary-layer flow is governed by the incompressible Navier–Stokes equations,¹⁷ given by:

$$\frac{u}{r} + \frac{\partial u}{\partial r} + \frac{1}{r} \frac{\partial v}{\partial \psi} + \frac{\partial w}{\partial z} = 0 \quad (1a)$$

$$\frac{\partial u}{\partial t} + u \frac{\partial u}{\partial r} + \frac{v}{r} \frac{\partial u}{\partial \psi} + w \frac{\partial u}{\partial z} - \frac{v^2}{r} = 2\Omega v - \frac{1}{\rho_0} \frac{\partial p}{\partial r} + \nu \left(\frac{\partial^2 u}{\partial r^2} + \frac{1}{r} \frac{\partial u}{\partial r} + \frac{1}{r^2} \frac{\partial^2 u}{\partial \psi^2} + \frac{\partial^2 u}{\partial z^2} - \frac{u}{r^2} - \frac{2}{r^2} \frac{\partial v}{\partial \psi} \right) \quad (1b)$$

$$\frac{\partial v}{\partial t} + u \frac{\partial v}{\partial r} + \frac{v}{r} \frac{\partial v}{\partial \psi} + w \frac{\partial v}{\partial z} + \frac{uv}{r} = 2\Omega u - \frac{1}{\rho_0 r} \frac{\partial p}{\partial \psi} + \nu \left(\frac{\partial^2 v}{\partial r^2} + \frac{1}{r} \frac{\partial v}{\partial r} + \frac{1}{r^2} \frac{\partial^2 v}{\partial \psi^2} + \frac{\partial^2 v}{\partial z^2} - \frac{v}{r^2} + \frac{2}{r^2} \frac{\partial u}{\partial \psi} \right) \quad (1c)$$

$$\frac{\partial w}{\partial t} + u \frac{\partial w}{\partial r} + \frac{v}{r} \frac{\partial w}{\partial \psi} + w \frac{\partial w}{\partial z} = g \left(\frac{\theta - \theta_0}{\theta_0} \right) - \frac{1}{\rho_0} \frac{\partial p}{\partial z} + \nu \left(\frac{\partial^2 w}{\partial r^2} + \frac{1}{r} \frac{\partial w}{\partial r} + \frac{1}{r^2} \frac{\partial^2 w}{\partial \psi^2} + \frac{\partial^2 w}{\partial z^2} \right) \quad (1d)$$

where u , v and w are the wind velocities in the radial, azimuthal and vertical directions, respectively. The Coriolis force is represented by $\Omega = \omega \sin \varphi$, where $\omega = 7.29 \times 10^{-5} \text{ rad s}^{-1}$ is the planetary rotation rate and φ the positional latitude; ρ_0 is the constant air density; p is the pressure; ν is the kinematic viscosity of air; g the gravitational acceleration; θ is the potential temperature given by $\theta = T - \Gamma_d z$, where T is the temperature and Γ_d is the dry adiabatic lapse rate and θ_0 is a reference temperature. In order to solve (1), boundary and initial conditions similar to those described in Section 2.2 are employed.

The momentum equations (1b)–(1d) describe how the three components of the wind, at each point within the flow, evolve over time in response to a number of forcing terms, such as the Coriolis force, pressure gradients, convection and diffusion. The flow is assumed to be incompressible (1a) with constant density, and so buoyancy effects arising from variable density are included via a Boussinesq approximation²⁹ that yields a buoyancy forcing term in the vertical momentum equation (1d).

3.2. Derivation of a low-order wind estimation model

From a mathematical perspective, the atmospheric boundary layer equations (1) are a coupled set of nonlinear partial differential-algebraic equations for which no analytic solution exists. Numerical solvers (e.g. SOWFA) must therefore be employed, and these commence from a spatial discretization of (1), whereby the velocity field is evaluated at a finite but large (e.g. $\mathcal{O}(10^7)$) set of grid points within the three-dimensional spatial domain. Solving (1) on such a large number of grid points is not practical from the point of view of real-time wind field estimation, and so we seek to derive models of significantly less complexity, proceeding from a scale analysis of (1).

3.2.1. Scale analysis.

In order to obtain a simplified dynamic wind model, we first seek to identify and retain only the dominant terms in (1). The analysis proceeds by defining the following characteristic scales of the wind field perturbations observed from LES data.

$$\begin{aligned} U &\sim 10^1 \text{ ms}^{-1} && \text{radial, azimuthal velocity scale,} \\ W &\sim 10^{-2} \text{ ms}^{-1} && \text{vertical velocity scale,} \\ L &\sim 10^2 \text{ m} && \text{radial, azimuthal length scale,} \\ H &\sim 10 \text{ m} && \text{vertical length scale,} \\ L/U &\sim 10 \text{ s} && \text{time scale,} \\ \delta P &\sim 10^1 \text{ Pa} && \text{static pressure fluctuation scale,} \\ \frac{\delta \Theta}{\Theta} &\sim 10^{-1} && \text{relative temperature fluctuation scale} \end{aligned}$$

Table I. Scale analysis of the atmospheric boundary layer equations (1).

(1a)	$\frac{u}{r}$	$\frac{\partial u}{\partial r}$	$\frac{1}{r} \frac{\partial v}{\partial \psi}$	$\frac{\partial w}{\partial z}$										
Scales	$\frac{U}{L}$	$\frac{U}{L}$	$\frac{U}{L}$	$\frac{W}{H}$										
ms ⁻²	10 ⁻¹	10 ⁻¹	10 ⁻¹	10 ⁻³										
(1b)	$\frac{\partial u}{\partial t}$	$u \frac{\partial u}{\partial r}$	$\frac{v}{r} \frac{\partial u}{\partial \psi}$	$w \frac{\partial u}{\partial z}$	$\frac{v^2}{r}$	$2\Omega v$	$\frac{1}{\rho_0} \frac{\partial p}{\partial r}$	$v \frac{\partial^2 u}{\partial r^2}$	$\frac{v}{r} \frac{\partial u}{\partial r}$	$\frac{v}{r^2} \frac{\partial^2 u}{\partial \psi^2}$	$v \frac{\partial^2 u}{\partial z^2}$	$\frac{v u}{r^2}$	$\frac{2v}{r^2} \frac{\partial v}{\partial \psi}$	
Scales	$\frac{U^2}{L}$	$\frac{U^2}{L}$	$\frac{U^2}{L}$	$\frac{WU}{H}$	$\frac{U^2}{L}$	JU	$\frac{\delta P}{\rho_0 L}$	$\frac{vU}{L^2}$	$\frac{vU}{L^2}$	$\frac{vU}{L^2}$	$\frac{vU}{H^2}$	$\frac{vU}{L^2}$	$\frac{vU}{L^2}$	
ms ⁻²	10 ⁰	10 ⁰	10 ⁰	10 ⁻²	10 ⁰	10 ⁻³	10 ⁻¹	10 ⁻⁸	10 ⁻⁸	10 ⁻⁸	10 ⁻⁶	10 ⁻⁸	10 ⁻⁸	
(1c)	$\frac{\partial v}{\partial t}$	$u \frac{\partial v}{\partial r}$	$\frac{v}{r} \frac{\partial v}{\partial \psi}$	$w \frac{\partial v}{\partial z}$	$\frac{uv}{r}$	$2\Omega u$	$\frac{1}{\rho_0 r} \frac{\partial p}{\partial \psi}$	$v \frac{\partial^2 v}{\partial r^2}$	$\frac{v}{r} \frac{\partial v}{\partial r}$	$\frac{v}{r^2} \frac{\partial^2 v}{\partial \psi^2}$	$v \frac{\partial^2 v}{\partial z^2}$	$\frac{v v}{r^2}$	$\frac{2v}{r^2} \frac{\partial u}{\partial \psi}$	
Scales	$\frac{U^2}{L}$	$\frac{U^2}{L}$	$\frac{U^2}{L}$	$\frac{WU}{H}$	$\frac{U^2}{L}$	JU	$\frac{\delta P}{\rho_0 L}$	$\frac{vU}{L^2}$	$\frac{vU}{L^2}$	$\frac{vU}{L^2}$	$\frac{vU}{H^2}$	$\frac{vU}{L^2}$	$\frac{vU}{L^2}$	
ms ⁻²	10 ⁰	10 ⁰	10 ⁰	10 ⁻²	10 ⁰	10 ⁻³	10 ⁻¹	10 ⁻⁸	10 ⁻⁸	10 ⁻⁸	10 ⁻⁶	10 ⁻⁸	10 ⁻⁸	
(1d)	$\frac{\partial w}{\partial t}$	$u \frac{\partial w}{\partial r}$	$\frac{v}{r} \frac{\partial w}{\partial \psi}$	$w \frac{\partial w}{\partial z}$	$g \left(\frac{\theta - \theta_0}{\theta_0} \right)$	$\frac{1}{\rho_0} \frac{\partial p}{\partial z}$	$v \frac{\partial^2 w}{\partial r^2}$	$\frac{v}{r} \frac{\partial w}{\partial r}$	$\frac{v}{r^2} \frac{\partial^2 w}{\partial \psi^2}$	$v \frac{\partial^2 w}{\partial z^2}$				
Scales	$\frac{UW}{L}$	$\frac{UW}{L}$	$\frac{UW}{L}$	$\frac{W^2}{H}$	$g \frac{\delta \Theta}{\Theta}$	$\frac{\delta P}{\rho_0 H}$	$\frac{vW}{L^2}$	$\frac{vW}{L^2}$	$\frac{vW}{L^2}$	$\frac{vW}{H^2}$				
ms ⁻²	10 ⁻³	10 ⁻³	10 ⁻³	10 ⁻⁵	10 ⁰	10 ⁰	10 ⁻¹¹	10 ⁻¹¹	10 ⁻¹¹	10 ⁻⁹				

The static pressure fluctuations arise from spatial variations in air density within the atmosphere. The value listed in the previous discussion is consistent with that in¹⁷ and arises from the motion of large scale structures (e.g. eddies and thermals) within the boundary layer. The time scale defined in the previous discussion is an advective time scale that characterizes the time taken for a gust to move past a fixed point in space. With respect to the Coriolis forcing terms, it is convenient to consider synoptic motions centred at mid-latitude $\varphi = 45^\circ$ and define a further scaling:

$$J := 2\Omega = 2\omega \sin \varphi = 2\omega \cos \varphi \sim 10^{-4} \text{ s}^{-1}$$

Based on these characteristic scalings, Table I shows the typical magnitudes of each term in the atmospheric boundary layer equations (1).

Retaining only the leading order terms results in the following reduced set of equations:

$$\frac{u}{r} + \frac{\partial u}{\partial r} + \frac{1}{r} \frac{\partial v}{\partial \psi} = 0 \tag{2a}$$

$$\frac{\partial u}{\partial t} = -u \frac{\partial u}{\partial r} - \frac{v}{r} \frac{\partial u}{\partial \psi} + \frac{v^2}{r} \tag{2b}$$

$$\frac{\partial v}{\partial t} = -u \frac{\partial v}{\partial r} - \frac{v}{r} \frac{\partial v}{\partial \psi} - \frac{uv}{r} \tag{2c}$$

$$g \left(\frac{\theta - \theta_0}{\theta_0} \right) = \frac{1}{\rho_0} \frac{\partial p}{\partial z} \tag{2d}$$

Inspection of these equations reveals that the dynamics of the wind field in the horizontal plane (2b)-(2c) are largely independent of changes in pressure and height, and so the vertical momentum equation (2d) can be discarded, which represents a significant modelling simplification. It is also worth noting that the radial and azimuthal momentum equations (2b)-(2c) are comprised primarily of advective terms and are therefore consistent with Taylor's frozen turbulence hypothesis. However, it is important to point out that these equations are coupled and therefore can not be solved independently. Moreover, this coupling is an important feature of the wind dynamics in attempting to estimate the unmeasured azimuthal velocities from measurements of the radial velocity field. The coupling between the radial and azimuthal velocity fields can be enhanced by assuming that the instantaneous wind direction is uniform within the limited spatial domain under study (shown in Figure 4). To find the wind direction, the following equation is used:

$$\psi + \tan^{-1} \left(\frac{r v}{u} \right) = c(t) \tag{3}$$

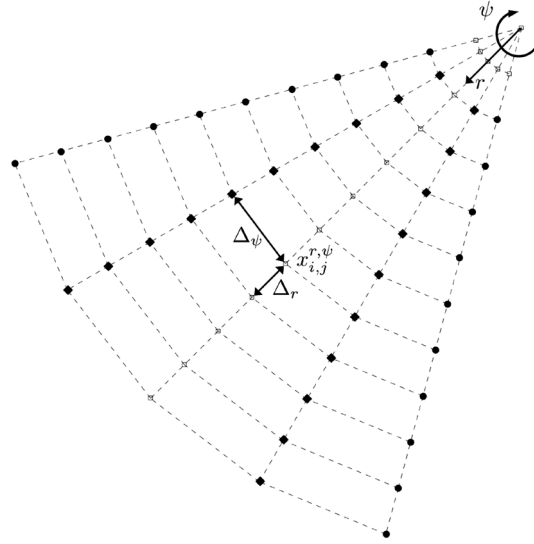


Figure 4. Spatial discretization of the estimation domain, and polar coordinate system. Solid circles ● indicate locations sampled by the 30° half-angle LiDAR case, whilst solid diamonds ◆ are locations sampled in the 15° half-angle case.

where $c(t)$ is the spatially averaged wind direction at each instant in time. This assumption is justified from inspection of LES data which points to a typical root-mean-squared (RMS) error of less than 2 degrees within the spatial domain spanned by the LiDAR beams. Without this assumption, the convergence properties of subsequent wind field estimates are adversely affected.

Further simplification of (2) is possible by redefining the velocities u and v in terms of a stream function $\phi(r, \psi, t)$ that implicitly satisfies the continuity equation (2a). A stream function that achieves this is as follows:

$$u := \frac{1}{r} \frac{\partial \phi}{\partial \psi}, \quad v := -\frac{\partial \phi}{\partial r} \tag{4}$$

Substituting into the u and v -momentum equations yields the following pair of coupled, nonlinear, partial differential equations:

$$\frac{\partial}{\partial t} \left(\frac{\partial \phi}{\partial r} \right) = -\frac{1}{r} \frac{\partial \phi}{\partial \psi} \frac{\partial^2 \phi}{\partial r^2} + \frac{1}{r} \frac{\partial \phi}{\partial r} \frac{\partial^2 \phi}{\partial r \partial \psi} - \frac{1}{r^2} \frac{\partial \phi}{\partial r} \frac{\partial \phi}{\partial \psi} \tag{5a}$$

$$\frac{\partial}{\partial t} \left(\frac{\partial \phi}{\partial \psi} \right) = \frac{1}{r^2} \left(\frac{\partial \phi}{\partial \psi} \right)^2 - \frac{1}{r} \frac{\partial \phi}{\partial \psi} \frac{\partial^2 \phi}{\partial r \partial \psi} + \frac{1}{r} \frac{\partial \phi}{\partial r} \frac{\partial^2 \phi}{\partial \psi^2} + \left(\frac{\partial \phi}{\partial r} \right)^2 \tag{5b}$$

Owing to their nonlinearity, it is necessary to solve these equations (subject to the directional constraint (3)) in a numeric fashion, and so we proceed to discretize (5) both spatially and temporally.

3.2.2. Spatio-temporal discretization.

We begin by defining the states of our system. Referring to (5), a natural choice for the states are $\mathbf{x}^r(r, \psi, t) := \frac{\partial \phi}{\partial r}$ and $\mathbf{x}^\psi(r, \psi, t) := \frac{\partial \phi}{\partial \psi}$. The stream function equations (5) are first rendered finite-dimensional via spatial discretization in the radial and azimuthal directions. Figure 4 shows the location of the chosen grid points within a conical domain of 30° half angle. The radial discretization consists of $N_r = 12$ grid points that are equally spaced according to the resolution of the LiDAR instrument, in this case by a distance of $\Delta_r = 20$ m apart.

In the azimuthal direction, there are $N_\psi = 5$ different ‘beams’ emanating from the origin, spaced apart in 15° increments. In the 30° LiDAR case, measurements are taken from the outer beams, whilst in the 15° half-angle case, measurements are taken on the second and fourth beams, as shown in Figure 4. The spacing between the azimuthal grid points is dependent on r , given by $\Delta_\psi = r \sin 15 / \sin 82.5 \approx 0.26r$. The discretized domain consists of 56 grid points, each characterized by radial and azimuthal indices, i and j respectively, where $i = 1, 2, \dots, 12$ and $j = 1, 2, \dots, 5$. Two states are defined at each grid point, $x_{i,j}^r(t)$ and $x_{i,j}^\psi(t)$ and these are stacked together as $\begin{bmatrix} x_{i,j}^r & x_{i,j}^\psi \end{bmatrix}^T$ to form the overall state vector of the system $x(t)$, consisting of a total of 112 individual states.

All gradient terms in (5) are approximated by a finite difference scheme, chosen for its simplicity of implementation. The partial derivatives with respect to time are discretized using a backwards Euler finite difference scheme, given by

$$\frac{\partial x_{i,j,k}^r}{\partial t} \approx \frac{1}{\Delta_t} (x_{i,j,k}^r - x_{i,j,k-1}^r) \quad (6)$$

where Δ_t represents the time step and similar expressions are chosen for the \mathbf{x}^ψ states. With respect to the spatial discretization of interior grid points, central finite differences are used, hence:

$$\frac{\partial x_{i,j,k}^r}{\partial r} \approx \frac{1}{2\Delta_r} (x_{i+1,j,k}^r - x_{i-1,j,k}^r) \quad (7a)$$

$$\frac{\partial x_{i,j,k}^r}{\partial \psi} \approx \frac{1}{2\Delta_\psi} (x_{i,j+1,k}^r - x_{i,j-1,k}^r) \quad (7b)$$

At points on the boundary where it is not possible to use central finite differences, either a forward or backwards finite difference scheme is applied, using the appropriate interior point. For example, for the radial partial derivative terms at the grid points furthest from the origin,

$$\frac{\partial x_{N_r,j,k}^r}{\partial r} \approx \frac{1}{2\Delta_r} (3x_{N_r,j,k}^r - 4x_{N_r-1,j,k}^r + x_{N_r-2,j,k}^r) \quad (8)$$

For $i = 1$ a singularity exists since $r = 0$, hence the two states at the origin are both treated as an average of the states at $i = 2$. The \mathbf{x}^r states for which there is no measurement are approximated by a weighted average of neighbouring states in order to improve the coupling of information from adjacent beams where measurements are taken. To achieve this, the projection of the states $\begin{bmatrix} x_{i,j,k}^r \\ x_{i,j,k}^\psi \end{bmatrix}$ from one beam to another are required. As an example, for the point on the centre beam highlighted in Figure 4, the averaging is given by the following expression, in which $\{i,j\} = \{8,3\}$:

$$x_{i,j,k}^r = \frac{1}{5} (x_{i,j,k}^r + x_{i-1,j,k}^r + x_{i+1,j,k}^r + (x_{i,j-1,k}^r + x_{i,j+1,k}^r) \cos(15^\circ) + (x_{i,j+1,k}^\psi - x_{i,j-1,k}^\psi) r \cos(75^\circ)) \quad (9)$$

Upon spatio-temporal discretization, the discretized wind field, characterized by the state vector x_k , therefore evolves according to a set of first-order, nonlinear ordinary-difference equations of the form:

$$x_k = f(x_{k-1}) \quad (10a)$$

In order to complete the description of our system, a model relating the vector of LiDAR measurements y_k to the states is required. This can be expressed by the following linear equation:

$$y_k = Hx_k, \quad (10b)$$

where H is a matrix containing $1/r$ terms in relation to $x_{i,j}^\psi$ states, for $i = 3, 4, \dots, 12$ and $j = 1, 5$, and zeros everywhere else, for the 30° LiDAR half-angle case, and is similar for the 15° case with the exception that $j = 2, 4$. We note at this point that (10b) can be modified to include additive noise to model the effects of imperfect measurements, as will be discussed in more detail in Section 5.4. The system model (10) is now of a standard form to enable the design of a state estimator.

4. UNSCENTED KALMAN FILTER

Owing to the nonlinearity of the state equation (10a), an unscented Kalman filter (UKF)³⁰ is employed to estimate the states of the system, and hence the wind field. The advantages of the UKF over other nonlinear estimation techniques, such as the extensively used extended Kalman filter, are discussed in.³¹ We briefly summarize the UKF algorithm, and begin by defining the initial state estimate of the system $\hat{x}(0) := \hat{x}_0$. In practice, the initial state of the wind is not known, and so we set the state estimate vector to zero. Associated with this initial state is an initial state error covariance matrix $P_0 := \mathcal{E} \left\{ (x_0 - \hat{x}_0) (x_0 - \hat{x}_0)^T \right\}$, and is set to 0.1 times an identity matrix of length n , where n is the state dimension. We also define a square matrix \hat{X}_0 whose columns consist of concatenated state-estimate vectors, i.e.,

$$\hat{X}_0 := [\hat{x}_0 \ \dots \ \hat{x}_0] \quad (11)$$

At each sample instant $k \geq 1$, the UKF algorithm proceeds by constructing a matrix \mathcal{X}_{k-1} consisting of so-called sigma points that are essentially a collection of perturbed state vectors:

$$\mathcal{X}_{k-1} := [\hat{x}_{k-1} \hat{X}_{k-1} + \gamma \sqrt{P_{k-1}} \hat{X}_{k-1} - \gamma \sqrt{P_{k-1}}] \quad (12a)$$

where the scalar constant γ is defined in the succeeding discussion. Each column of this matrix is propagated according to the nonlinear state equation (10a) to yield an updated sigma point matrix $\mathcal{X}_{k|k-1}^-$, from which an updated state vector and covariance matrix can be computed, according to the following expressions:

$$\mathcal{X}_{k|k-1}^- = f(\mathcal{X}_{k-1}) \quad (12b)$$

$$\hat{x}_k^- = \sum_{l=1}^{2n+1} w_l^m \mathcal{X}_{l,k|k-1}^- \quad (12c)$$

$$P_k^- = \sum_{l=1}^{2n+1} w_l^c (\mathcal{X}_{l,k|k-1}^- - \hat{x}_k^-) (\mathcal{X}_{l,k|k-1}^- - \hat{x}_k^-)^T + R_w \quad (12d)$$

where $\gamma = \alpha^2(n + \kappa) - n$ is a constant in which α changes the spread of the sigma points and κ is a scaling factor. In the present study, $\alpha = 1$ and $\kappa = 3 - n$ were found sufficient. The notation \mathcal{X}_l denotes the l -th column of matrix \mathcal{X} , and R_w is the process-noise covariance, which can be computed from LES data. The wind direction correction step (3) is incorporated into step (12b) shown in the previous discussion. The scalar weights w_1^m , w_1^c , w_l^m and w_l^c are defined as follows:

$$w_1^m = \frac{\gamma}{n + \gamma} \quad (12e)$$

$$w_1^c = \frac{\gamma}{n + \gamma} + (1 - \alpha^2 + \beta) \quad (12f)$$

$$w_l^m = w_l^c = \frac{1}{2(n + \gamma)}, \quad l = 2, \dots, 2n + 1 \quad (12g)$$

where β is used to incorporate any prior knowledge of the states and was set to $\beta = 2$ in the present study. The next step involves augmenting the updated state estimate to include sigma points derived from the matrix square root of the state covariance matrix. Note that this additional step is only necessary when initially considering the zero mean noise case. The sigma points are then mapped according to the measurement equation (10b) to yield estimates \hat{y}_k of the LiDAR measurements. As with the states, the mean and covariance of the measurements are evaluated after mapping. Hence, these steps are given by:

$$\mathcal{X}_{k|k-1} = [\hat{x}_k^- \hat{X}_k^- + \gamma \sqrt{P_k^-} \hat{X}_k^- - \gamma \sqrt{P_k^-}] \quad (12h)$$

$$\mathcal{Y}_{k|k-1} = H \mathcal{X}_{k|k-1} \quad (12i)$$

$$\hat{y}_k^- = \sum_{l=1}^{2n+1} w_l^m \mathcal{Y}_{l,k|k-1} \quad (12j)$$

$$P_{y_k y_k} = \sum_{l=1}^{2n+1} w_l^c (\mathcal{Y}_{l,k|k-1} - \hat{y}_k^-) (\mathcal{Y}_{l,k|k-1} - \hat{y}_k^-)^T + R_v \quad (12k)$$

where R_v is the measurement noise covariance, and \hat{X}_k^- is the square matrix whose columns consist of concatenated state-estimate vectors, i.e.,

$$\hat{X}_k^- := [\hat{x}_k^- \cdots \hat{x}_k^-] \quad (12l)$$

where \hat{x}_k^- is computed from (12c). The remaining steps are the Kalman Filter update steps, consisting of:

$$P_{x_k y_k} = \sum_{l=1}^{2n+1} w_l^c (\mathcal{X}_{l,k|k-1} - \hat{x}_k^-) (\mathcal{Y}_{l,k|k-1} - \hat{y}_k^-)^T \quad (12m)$$

$$L_k = P_{x_k y_k} P_{y_k y_k}^{-1} \quad (12n)$$

$$\hat{x}_k = \hat{x}_k^- + L_k (y_k - \hat{y}_k^-) \quad (12o)$$

$$P_k = P_k^- - L_k P_{y_k y_k} L_k^T \quad (12p)$$

From the point of view of real-time application, each iteration of the UKF algorithm (12) is required to execute within a sample period, in this case 1 s, as dictated by the sampling capability of the LiDAR unit. The primary computational bottleneck in (12) is the solution of (12b). However, numerical tests revealed that a single iteration of the algorithm yielded an average run time of 0.0133 seconds*, which comfortably allows for real-time execution.

5. LIDAR WIND FIELD ESTIMATION: RESULTS AND DISCUSSION

5.1. Case 1: various half angles, fixed look direction, neutral atmospheric stability

The first case under study offers a comparison between wind field estimates produced by two different LiDAR configurations that differ with respect to the beam half-angle. The first configuration has a beam half-angle of 15°, whilst the second configuration has a wider half-angle of 30°. The domain of estimation is the same in both cases, namely a conical sector of half-angle 30° and a radius of 220 m. The LiDAR instrument is pointed directly into a neutrally stable wind field with a mean direction of 225°. Two separate UKFs were synthesized for each configuration, with the only difference being the sensor matrix H in (10b), reflecting the fact that measurements are taken at different locations within the wind field. Both filters were seeded with the same initial state estimate, specifically an initial estimate of zero for each state, corresponding to a quiescent wind field. Such a poor initial estimate was deliberately chosen to emphasize the subsequent convergence of the state estimates upon subsequent iterations of the filter algorithms. A total of 230 s worth of LES data was generated, providing each filter with 230 time samples of the radial component of the wind field along the LiDAR beams. At each sample instant, these measurements of the wind field were supplied to the UKF algorithms in order to generate estimates of the full state vector, which could then be plotted to visualize the wind magnitude and direction. Examples of these plots are displayed in Figure 5 at four separate times $t = \{0, 1, 10, 30\}$ s. The left-hand plots show the actual wind field, as produced by the LES simulations, at these times, whilst the central and right-hand plots show the corresponding estimated wind fields for the 15° and 30° LiDAR half-angle cases, respectively.

At $t = 0$ s (top row), the UKFs initiate from the quiescent initial state estimate, which is clearly erroneous compared to the actual wind field. At $t = 1$ s (second row), the filters have received a single time sample of the radial wind field along the LiDAR beams, enabling the initial state estimate to be updated. Immediately, we see a drastic improvement in the state estimates along the LiDAR beams, with the magnitude and direction of the wind starting to closely match the actual wind field at the locations where LiDAR measurements are taken. After just one iteration however, not enough time has elapsed for information from the LiDAR measurements to propagate through to the rest of the spatial domain, and so, the off-beam states remain largely quiescent. This situation does not last long, however, and after just 10 updates of the UKF algorithm, at $t = 10$ s, the LiDAR measurements have propagated throughout the domain according to the dynamic wind model employed in the filters. From a qualitative perspective, the estimated wind field in the 15° case is in good agreement with the actual wind field and has detected the presence of a high-speed gust of magnitude approximately 10 m s^{-1} entering the estimation domain at a bearing of 210° and a low-speed gust of magnitude approximately 6 m s^{-1} entering from a bearing of 240°. The spatially averaged estimate of the wind direction is also in good agreement. The estimates from the 30° case are somewhat poorer at this point, with the estimated wind field failing to qualitatively match the actual wind field, in terms of magnitude at off-beam locations. This is perhaps to be expected given the greater separation between the LiDAR beams in this case. At $t = 30$ s (bottom row), the gusts have advanced from the southwest and are now significantly closer to the origin in the estimation domain. Again, the qualitative picture from the 15° case is in reasonable agreement with respect to the location, magnitude and direction of these gusts, whilst the 30° case is showing signs of improvement.

Quantitatively, it is instructive to compute the spatial RMS error of the estimated magnitudes as a function of time sample, in order to assess the convergence of the filters. This RMS error, as a function of the states, is defined as follows:

$$\text{RMS error } (k) := \sqrt{\frac{1}{N} \sum_{i=1}^{N_r} \sum_{j=1}^{N_\psi} \left(\sqrt{\left(\frac{x_{i,j,k}^\psi}{r} \right)^2 + (r x_{i,j,k}^r)^2} - \sqrt{\left(\frac{\hat{x}_{i,j,k}^\psi}{r} \right)^2 + (r \hat{x}_{i,j,k}^r)^2} \right)^2} \quad (13)$$

*All computations were performed on a 3.30GHz Quad Core Intel Xeon CPU machine, running MATLAB 2012b using IEEE double precision arithmetic with relative machine precision $\epsilon = 2.22 \times 10^{-16}$.

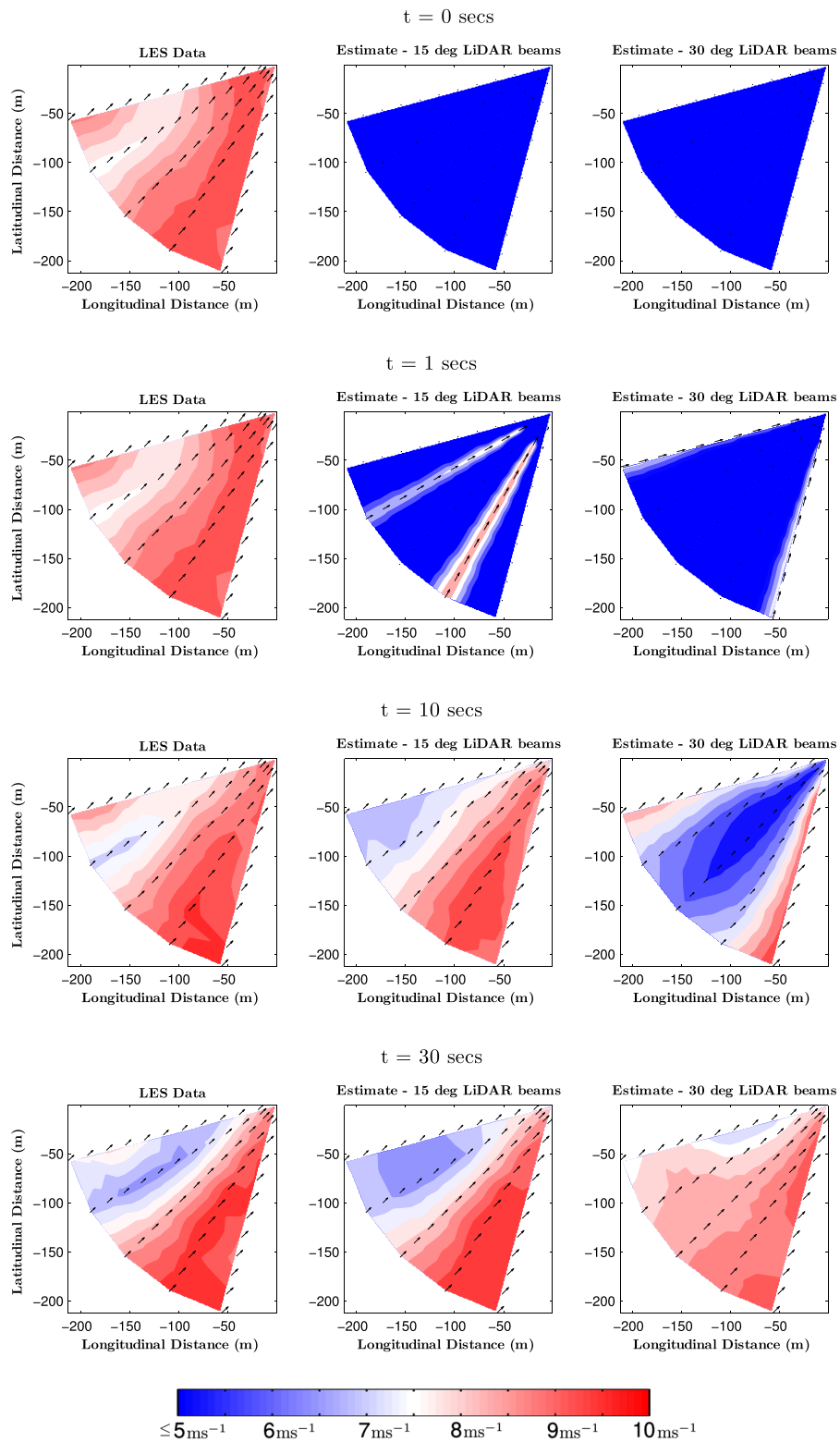


Figure 5. State estimation of an evolving wind field using 15° and 30° half-angle LiDAR beam configurations.

where N is the total number of grid points, and the point at the origin is treated according to earlier remarks in Section 3. This RMS error is plotted in Figure 6, which shows that estimates from the 15° case have largely converged after 10 iterations, and from thereon, the RMS error in the estimates is approximately 0.25 m s^{-1} . The estimates in the 30° case take a little longer to converge, and after 20 iterations, the errors settle to within 0.5 m s^{-1} . It is also instructive to consider the error in the spatially averaged estimate of the wind direction. Figure 7 displays the spatially averaged wind direction

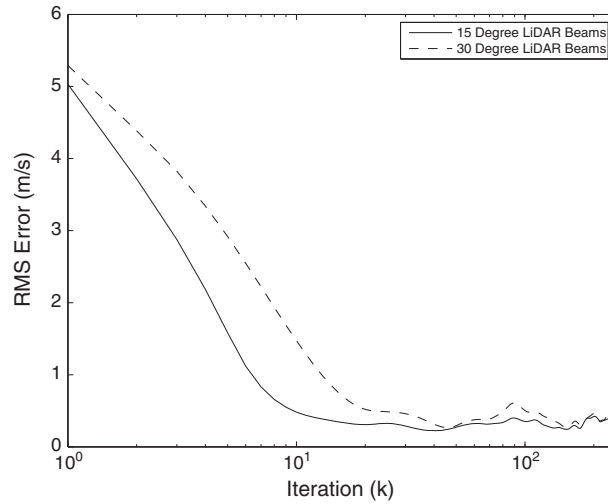


Figure 6. Semi-log plot of the RMS magnitude error for each LiDAR beam configuration.

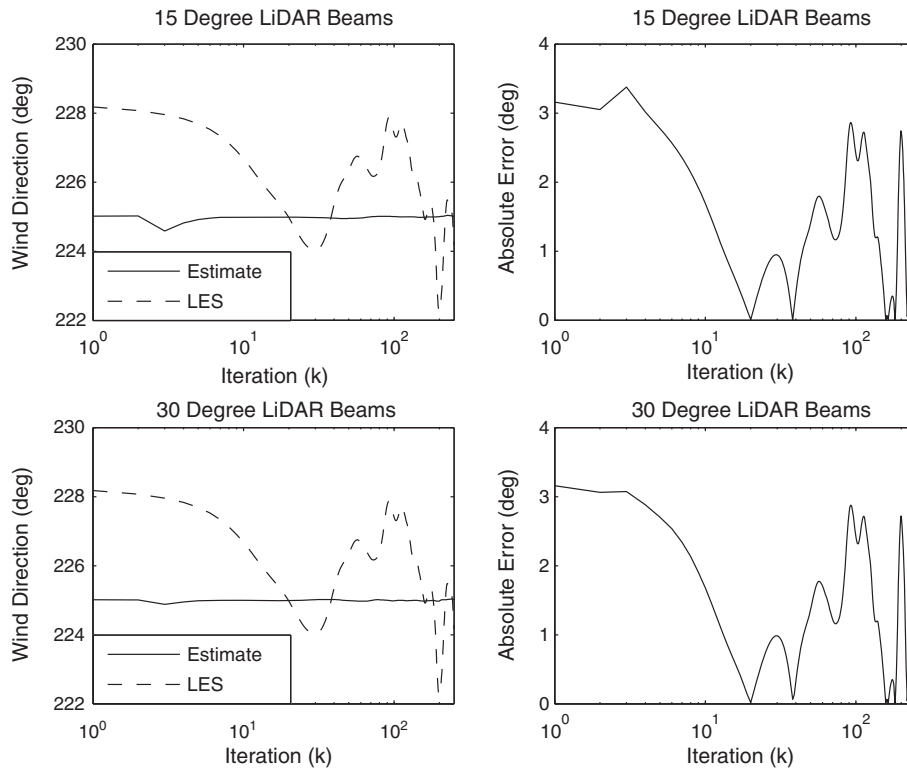


Figure 7. Performance of the wind direction estimates under neutral atmospheric stability conditions for different LiDAR half-angle configurations. The left-hand plots show the spatially averaged wind direction estimates in comparison to the spatially averaged wind direction from LES data, whilst the right hand plots show the absolute estimation error.

estimate compared to the actual averaged wind direction from LES data (left-hand plots) for the 15° (top row) and 30° (bottom row) cases. Almost immediately, the mean direction estimates tend towards the actual mean direction with the absolute error typically within 3°, in both cases.

5.2. Case 2: fixed half-angle, various look directions, neutral atmospheric stability

In this second case, we restrict attention to the 15° LiDAR half-angle configuration under conditions of neutral atmospheric stability but now vary the direction of the LiDAR beams with respect to the prevailing wind. In the first case in the previous discussion, the LiDAR instrument was pointed directly into the oncoming wind (from the southwest) but we now point the LiDAR in two different directions on either side of this, firstly towards the south, and secondly towards the west. The intention is to show that regardless of LiDAR misalignment with the oncoming wind, the estimation technique is sufficiently robust to accurately determine the wind magnitude and direction. Again, the UKF is seeded with a zero initial estimate on all states before being iterated over the simulation time horizon. Figure 8 shows the actual (left-hand plots) and estimated (right-hand plots) wind fields for the south-facing (top row) and west-facing (bottom row) cases at time $t = 230$ s when the filter transients have decayed away. Clearly, the estimated wind fields closely match the actual wind fields, both in terms of magnitude and direction. Figure 9 shows the RMS magnitude error. Although the transient behaviour differs,

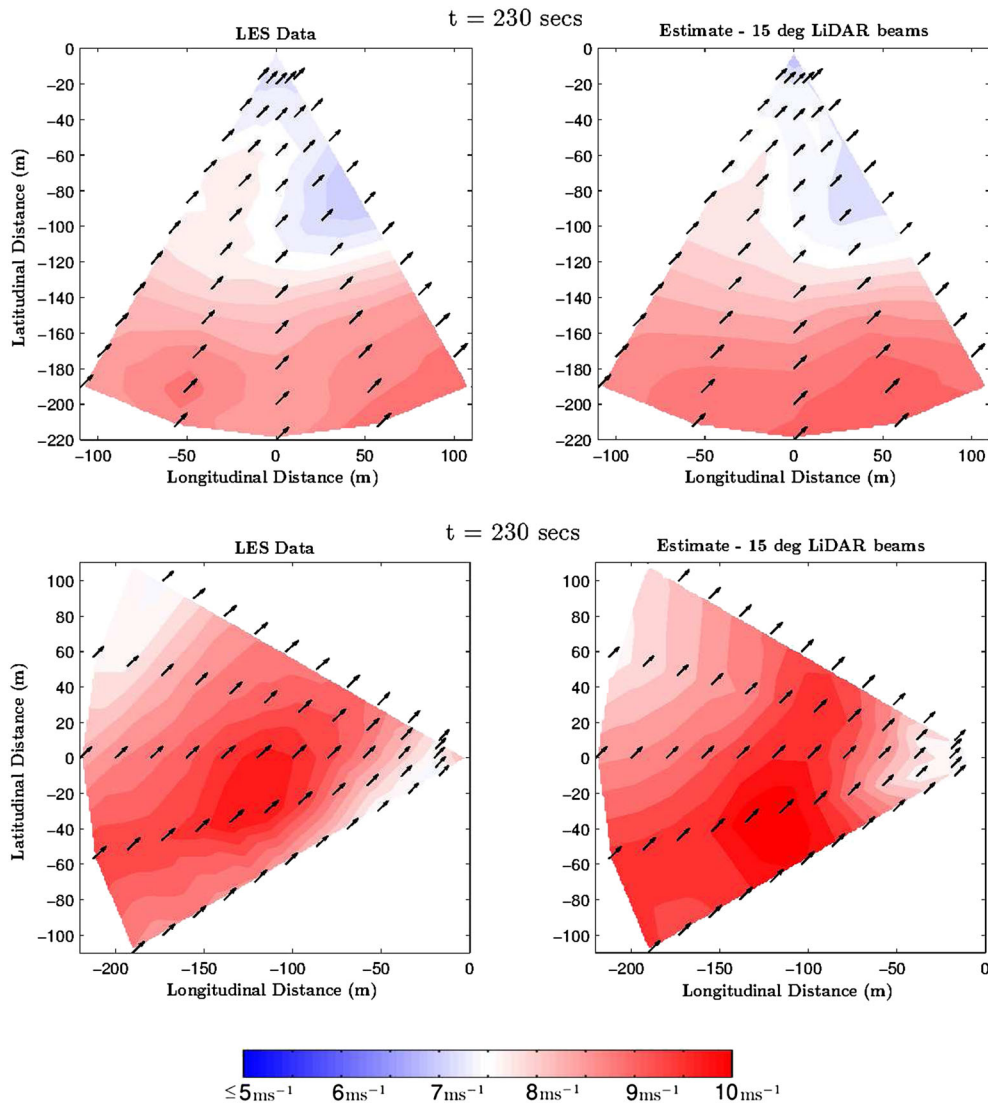


Figure 8. State estimation of an evolving wind field for LiDAR instruments facing away from the prevailing wind direction.

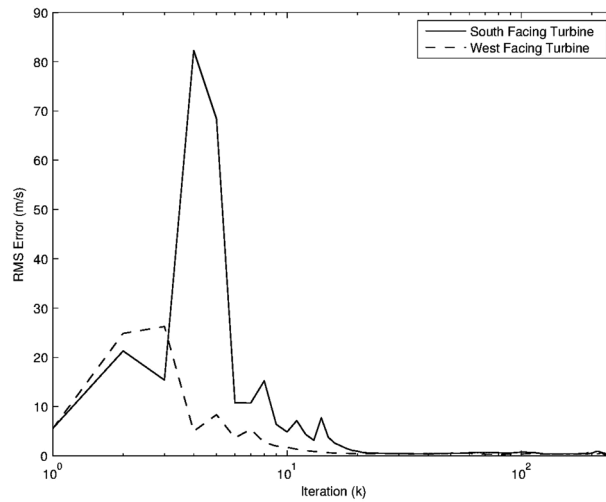


Figure 9. RMS magnitude error for both south-facing and west-facing LiDAR instruments. The prevailing wind is from the southwest.

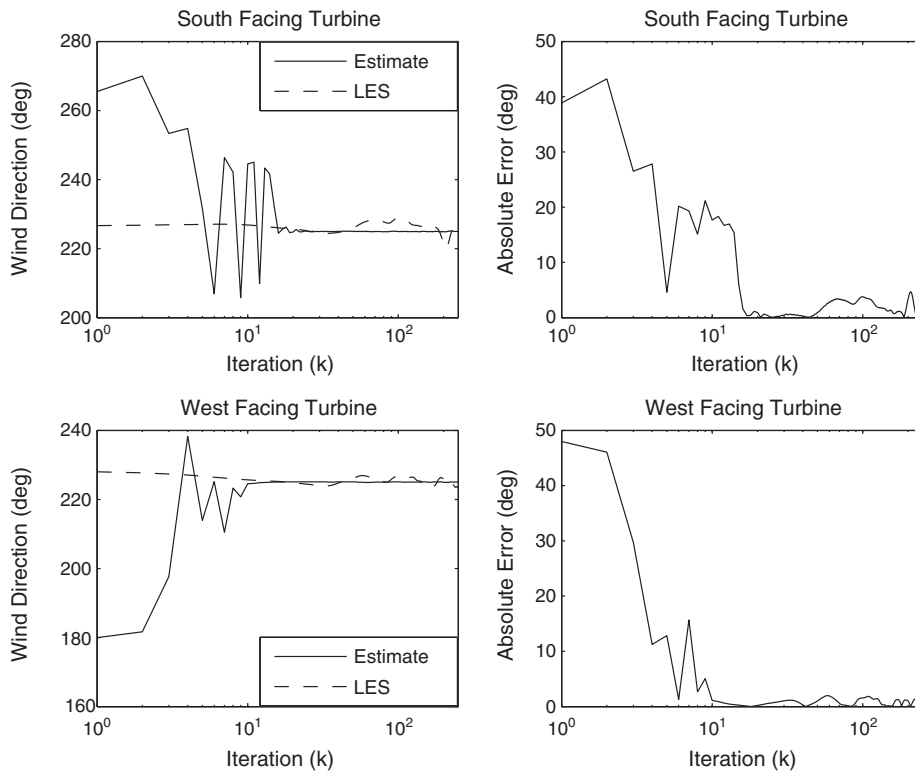


Figure 10. Spatially averaged wind direction estimates in comparison to the LES data (left-hand plots), together with the absolute error (right hand plots), under different LiDAR look directions.

after 20 iterations, the errors in both cases converge to within approximately 0.25 m s^{-1} , as in the southwest-facing case in the previous discussion. The wind direction errors for both cases are plotted in Figure 10 and again show convergence to within a few degrees. Clearly, after a brief transient period, the UKF begins to produce accurate estimates of the wind magnitude and direction, regardless of initial estimate or wind alignment. At this point we have therefore shown that this approach overcomes the cyclops dilemma.

5.3. Case 3: fixed half-angle, fixed look direction, various atmospheric stabilities

In this case, we employ a 15° LiDAR half-angle configuration pointing into the wind. We extract measurement data from simulations under, firstly, neutral and, secondly, unstable (reference temperature: $\theta_0 = 289$ K) atmospheric stability conditions. We would expect the estimates from the UKF to be insensitive to variations in atmospheric stability,

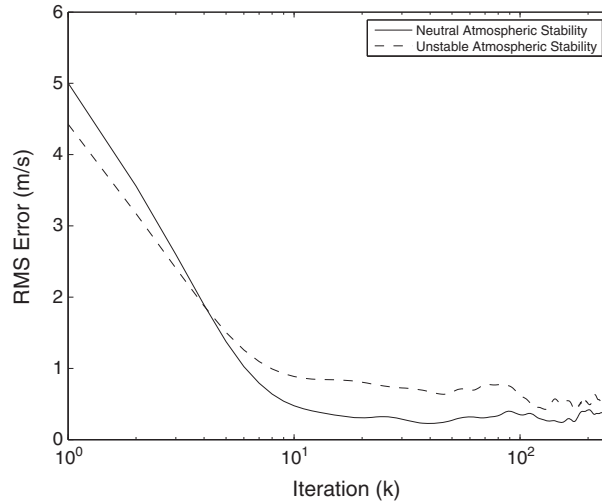


Figure 11. Semi-log plots of the RMS magnitude error for the neutral and unstable atmospheric stability cases.

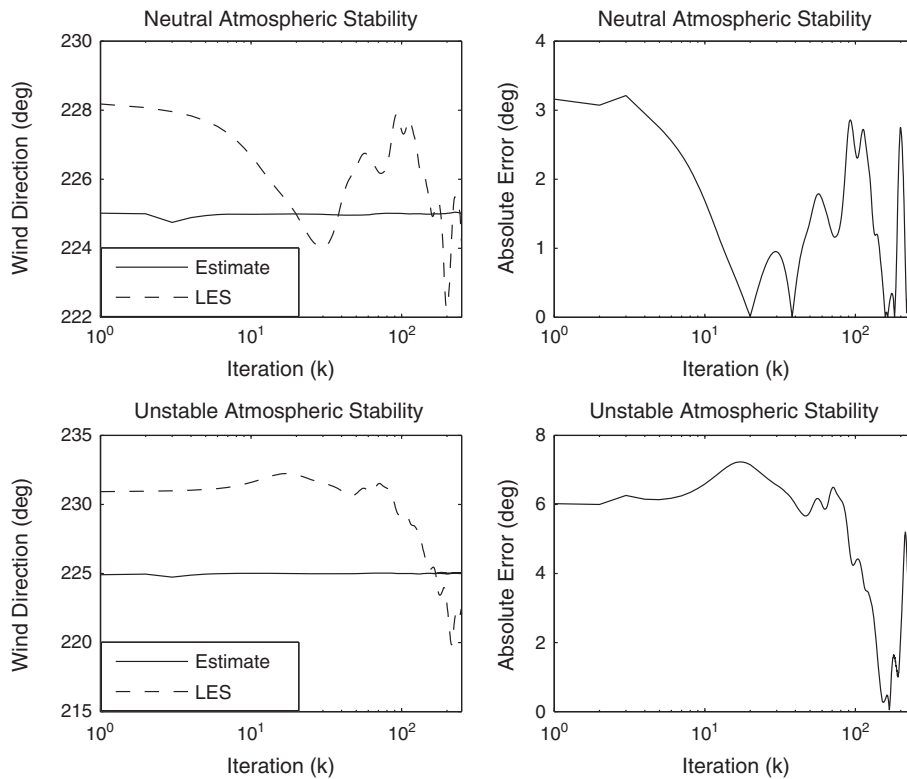


Figure 12. Spatially averaged wind direction estimates in comparison to the LES data (left-hand plots), together with the absolute error (right hand plots), for neutral and unstable atmospheric stability conditions.

partly according to the scale analysis arguments of Section 3.2.1, and also owing to the fact that the UKF employs measurement feedback and so we would expect to gain the benefits of feedback in the form of rejection of the effects of such parametric uncertainty upon the state estimates. The RMS magnitude error plot in Figure 11 indeed confirms this to be the case. Once the filter transients have died away after 20 iterations, there is little degradation in the estimates from the filter, regardless of whether it is being supplied measurements from a neutrally stable or unstable flow. Finally, Figure 12 shows the errors in the wind direction estimates. In the unstable case, the absolute wind direction error settles to within 5° of the actual value.

5.4. Case 4: fixed half-angle, fixed look direction, neutral atmospheric stability, various measurement noise

Up to this point the previous cases have each assumed the availability of ‘perfect’ LiDAR measurements in the sense that the assumed LiDAR instrument has provided the precise line-of-sight velocity at exact locations. This is of course not the case in practice. For instance, for continuous-wave LiDAR, the spatial averaging effect of range weighting results in the low-pass filtering of wind speeds, whilst velocity measurement from pulsed LiDAR requires a model of the pulse shape in order to determine a range weighting function,⁴ and such models will inevitably contain small errors. All of which and

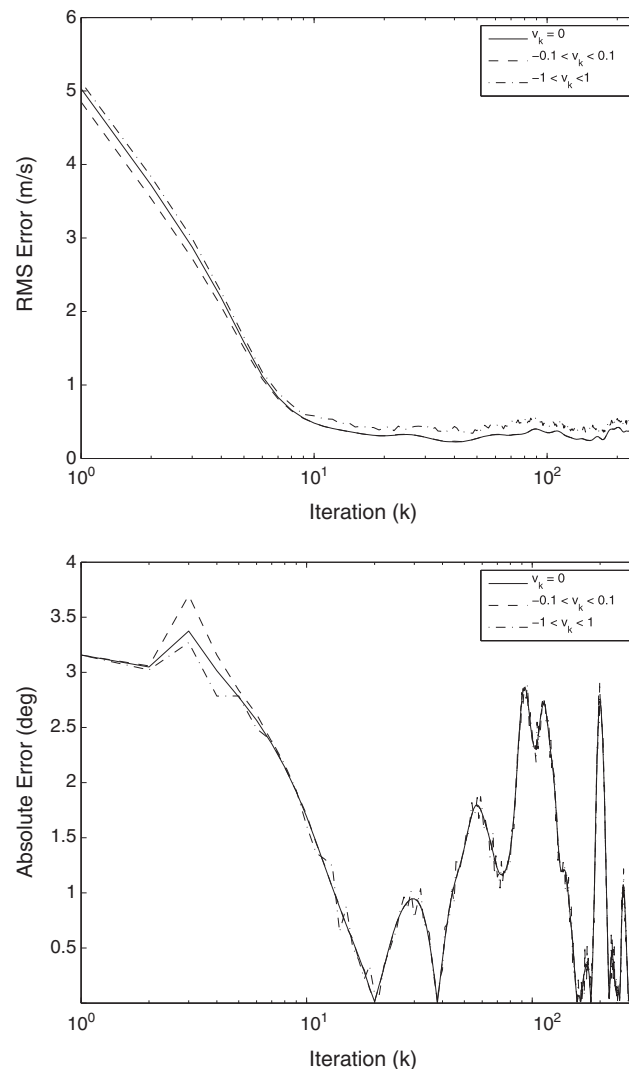


Figure 13. RMS magnitude errors (top plot) and absolute wind direction estimation errors (bottom plot) for the different measurement noise cases.

more, result in LiDAR measurements only being accurate to within a certain tolerance. Therefore, in this final case we explore the performance of the estimation scheme in the presence of imperfect measurements, assuming a 15° LiDAR half-angle configuration pointing into the wind under conditions of neutral atmospheric stability. We model imperfect measurements by modifying the measurement equation (10b) to include a noise vector v_k , as follows:

$$y_k = Hx_k + v_k \quad (14)$$

We consider two cases. Firstly, the case where the elements of v_k are drawn in random from the range $(-0.1, 0.1) \text{ m s}^{-1}$, and a second case where they are drawn from the range $(-1.0, 1.0) \text{ m s}^{-1}$. The first range is representative of the accuracy of commercially available pulsed LiDAR instruments, whilst the second is used to demonstrate the performance of the estimation technique using a considerably less accurate system. In both cases, knowledge of such imperfect measurements can be included in the measurement noise model of the UKF, specifically by modifying the diagonal elements of the measurement noise covariance matrix R_v in (12k) to include the variance of v_k . Figure 13 shows the RMS wind magnitude errors in both cases, as well as the absolute wind direction errors. Even in the noisier measurement case, both plots show little degradation compared to the case of perfect measurement ($v_k = 0$), suggesting insensitivity of the UKF to this source of measurement error. This is entirely to be expected given the UKF's use of feedback to disambiguate the measurement estimate from the corrupted measurements via knowledge of the system dynamics (10) and noise statistics (v_k in (14)).

Of course, there are many other potential sources of measurement error, such as tilt misalignment of the LiDAR instrument, as well as random loss of data at certain ranges, all of which would require careful consideration for eventual practical adoption of the estimation scheme detailed in this paper. We leave such issues to future studies.

6. CONCLUSIONS

We have shown in this paper that it is possible to compute estimates of the radial and azimuthal components of the wind field using only limited radial velocity measurements along two LiDAR beams. The consequences of this are twofold. Firstly, since the determination of both velocity components is equivalent to estimating the wind magnitude and direction, we have shown that it is possible to overcome the cyclops dilemma using dual-beam LiDAR. Secondly, and perhaps more importantly, we have developed a technique that can pinpoint the strength, location and direction of advancing gusts, with considerable accuracy. Results were presented that showed wind magnitudes and directions being estimated typically to within 0.5 m s^{-1} and 3 degrees of their respective values generated from high fidelity LES simulations, irrespective of unknown initial conditions. The key to producing such estimates lay firstly in the derivation of a simplified dynamic model of the atmospheric boundary layer that linked the LiDAR samples to the unmeasured velocities within the spatial domain under study, and secondly, the use of a state estimator to exploit the information contained within the temporal history of the LiDAR measurements. From a practical point of view, the use of a simplified model enabled estimates to be computed faster than the sample rate of the LiDAR instrument studied, thus paving the way for use in real-time applications.

The ability to accurately reconstruct an oncoming wind field in an efficient fashion has immediate relevance for a number of applications including improved site assessment and enhanced safety of construction and maintenance operations. Further refinement of this technique might also lead to improved power curve assessment and control to counter yaw misalignment. In terms of potential load reductions, knowledge of oncoming gusts could pave the way for preview action to be built into new or existing pitch control schemes (e.g.³²) for enhanced fatigue and extreme load rejection. Such avenues will be explored in future work.

ACKNOWLEDGEMENTS

The authors wish to express their thanks to Robert Bowyer and Chris Spruce of Vestas for their invaluable input, as well as the Engineering and Physical Sciences Research Council (EPSRC) for funding this project on grant EP/K007386/1.

REFERENCES

1. Fichaux N, Wilkes J, Oceans of opportunity - harnessing Europe's largest domestic energy resource. *Offshore Report*, The European Wind Energy Association, 2009.
2. Courtney M, Wagner R, Lindelöw P. Testing and comparison of lidars for profile and turbulence measurements in wind energy. *IOP Conference Series: Earth and Environmental Science* 2008; **1**(1): 1–14.
3. Mikkelsen T, Hansen KH, Angelou N, Sjöholm M, Harris M, Hadley P, Scullion R, Ellis G, Vives G. Lidar wind speed measurements from a rotating spinner. *2010 European Wind Energy Conference and Exhibition*, Warsaw, Poland, 2010; 1–8.

4. Dunne F, Simley E, Pao LY. Lidar wind speed measurement analysis and feed-forward blade pitch control for load mitigation in wind turbines. *Report NREL/SR-5000-52098*, NREL, 2011.
5. Soltani M, Wisniewski R, Brath P, Boyd S. Load reduction of wind turbines using receding horizon control. *2011 IEEE International Conference on Control Applications (CCA)*, IEEE, Denver, CO, 2011; 852–857.
6. Wang N, Johnson KE, Wright AD. FX-RLS-based feedforward control for LIDAR-enabled wind turbine load mitigation. *IEEE Transactions on Control Systems Technology* 2012; **20**(5): 1212–1222, DOI: 10.1109/TCST.2011.2163515.
7. Schlipf D, Schlipf DJ, Kühn M. Nonlinear model predictive control of wind turbines using LIDAR. *Wind Energy* 2013; **16**(7): 1107–1129.
8. Pao LY, Johnson KE. A tutorial on the dynamics and control of wind turbines and wind farms. *American Control Conference, 2009. ACC '09*, St. Louis, MO, 2009; 2076–2089.
9. Kelley ND, Osgood RM, Bialasiewicz JT, Jakubowski A. Using wavelet analysis to assess turbulence/rotor interactions. *Wind Energy* 2000; **3**: 121–134.
10. Hand MM. Mitigation of wind turbine/vortex interaction using disturbance accommodating control, *Ph.D. Thesis*, Colorado, USA, 2003.
11. Harris M, Bryce DJ, Coffey AS, Smith DA, Birkemeyer J, Knopf U. Advance measurement of gusts by laser anemometry. *Journal of Wind Engineering and Industrial Aerodynamics* 2007; **95**(12): 1637–1647.
12. Angelou N, Mann J, Courtney M, Sjöholm M. Doppler lidar mounted on a wind turbine nacelle – UPWIND deliverable D6.7.1. *Technical Report Risø-R-1757 (EN)*, RisøDTU, 2010.
13. Simley E, Pao L, Frehlich R, Jonkman B, Kelley N. Analysis of wind speed measurements using continuous wave LIDAR for wind turbine control. *49th AIAA Aerospace Sciences Meeting Including the New Horizons Forum and Aerospace Exposition*, American Institute of Aeronautics and Astronautics, Orlando, Florida, 2011; 1–16.
14. Mikkelsen T, Angelou N, Hansen K, Sjöholm M, Harris M, Slinger C, Hadley P, Scullion R, Ellis G, Vives G. A spinner-integrated wind lidar for enhanced wind turbine control. *Wind Energy* 2013; **16**(4): 625–643.
15. Taylor GI. The spectrum of turbulence. *Proceedings of the Royal Society of London. Series A-Mathematical and Physical Sciences* 1938; **164**(919): 476–490.
16. Raach S, Schlipf D, Haizmann F, Cheng PW. Three dimensional dynamic model based wind field reconstruction from lidar data. *Journal of Physics: Conference Series* 2014; **524**(1): 012005. DOI: 10.1088/1742-6596/524/1/012005. [Online]. Available: <http://stacks.iop.org/1742-6596/524/i=1/a=012005>. (Accessed 29 October 2014).
17. Stull RB. *An Introduction to Boundary Layer Meteorology*, Vol. 13. Springer: New York City, 1988.
18. Soleimanzadeh M, Wisniewski R, Brand A. State-space representation of the wind flow model in wind farms. *Wind Energy* 2014; **17**(4): 627–639.
19. Wan EA, Merwe RVD. The unscented Kalman filter for nonlinear estimation. *Adaptive Systems for Signal Processing, Communications, and Control Symposium 2000. AS-SPCC*, IEEE, Lake Louise, Alta, 2000; 153–158.
20. Kalman RE. A new approach to linear filtering and prediction problems. *Journal of Basic Engineering* 1960; **82**(1): 35–45.
21. Åström KJ, Murray RM. *Feedback Systems: An Introduction for Scientists and Engineers*. Princeton University Press: Princeton, NJ, 2008.
22. Anderson BDO, Moore JB. *Optimal Filtering*, Dover books on engineering. Dover Publications, 2005.
23. Gelb A. *Applied Optimal Estimation*. MIT Press: Cambridge, MA, 1999.
24. Green M, Limebeer DJN. *Linear Robust Control*. Prentice-Hall, Inc.: NJ, USA, 1995.
25. Churchfield MJ, Lee S. SOWFA, NWTC design codes, NREL. *19th Symposium on Boundary Layers and Turbulence*, Keystone, CO, 2012; 1–23. [Online]. Available: <http://wind.nrel.gov/designcodes/simulators/SOWFA/>.
26. Churchfield MJ, Moriarty PJ, Vijayakumar G, Brasseur J. *Wind energy-related atmospheric boundary-layer large-eddy simulation using openfoam*, 2010.
27. Churchfield MJ, Lee S, Michalakes J, Moriarty PJ. A numerical study of the effects of atmospheric and wake turbulence on wind turbine dynamics. *Journal of Turbulence* 2012; **13**: 1–32.
28. Moeng CH. A large-eddy-simulation model for the study of planetary boundary-layer turbulence. *Journal of the Atmospheric Sciences* 1984; **41**(13): 2052–2062.
29. Holton JR, Hakim GJ. *An Introduction to Dynamic Meteorology* (5th edn.) Academic press: Waltham, MA, 2012.
30. Julier SJ, Uhlmann JK. Unscented filtering and nonlinear estimation. *Proceedings of the IEEE* 2004; **92**(3): 401–422.
31. Haykin SS. *Kalman Filtering and Neural Networks*. Wiley Online Library: Hoboken, NJ, 2001.
32. Lu Q, Bowyer R, Jones BLI. Analysis and design of Coleman transform-based individual pitch controllers for wind-turbine load reduction. *Wind Energy* 2014, DOI: 10.1002/we.1769.